

**R. Balderrama**  
Mechanical Engineering School,  
Universidad Central de Venezuela,  
Caracas, Venezuela

**A. P. Cisilino<sup>1</sup>**  
Department of Mechanical Engineering,  
Welding and Fracture Division – INTEMA –  
CONICET,  
Universidad Nacional de Mar del Plata,  
Av. Juan B. Justo 4302,  
7600 Mar del Plata,  
Argentina  
e-mail: cisilino@fi.mdp.edu.ar

**M. Martinez**  
Mechanical Engineering School,  
Universidad Central de Venezuela,  
Caracas, Venezuela

# Boundary Element Method Analysis of Three-Dimensional Thermoelastic Fracture Problems Using the Energy Domain Integral

*A boundary element method (BEM) implementation of the energy domain integral (EDI) methodology for the numerical analysis of three-dimensional fracture problems considering thermal effects is presented in this paper. The EDI is evaluated from a domain representation naturally compatible with the BEM, since stresses, strains, temperatures, and derivatives of displacements and temperatures at internal points can be evaluated using the appropriate boundary integral equations. Special emphasis is put on the selection of the auxiliary function that represents the virtual crack advance in the domain integral. This is found to be a key feature to obtain reliable results at the intersection of the crack front with free surfaces. Several examples are analyzed to demonstrate the efficiency and accuracy of the implementation. [DOI: 10.1115/1.2173287]*

## 1 Introduction

Assessing the engineering integrity and life expectancy of thermally stressed components, either under service conditions or during the design stage, requires the determination of fracture parameters. Over the years much work has been done to evaluate stress intensity factors for these problems, resulting in collections of results published in handbook form [1,2]. However, most of these solutions are restricted to regular cracks in infinite or semi-finite solids and two-dimensional simple crack geometries. The solution of complicated three-dimensional crack problems usually requires such numerical techniques as the finite element method (FEM) and the boundary element method (BEM).

The attraction of the BEM can be largely attributed to the reduction in the dimensionality of the problem; for three-dimensional problems only the surface of the domain needs to be discretized [3]. At the same time, and due to the inherent characteristics of its formulation, the BEM provides very accurate results for problems containing strong geometrical discontinuities. This makes the BEM a powerful numerical tool for modeling crack problems [4]. In particular, thermoelastic BEM formulations have been presented, among others, by Raveendra and Banerjee [5], Mukherjee et al. [6], Prasad et al. [7], and dell'Erba and Aliabadi [8].

Evaluation of stress intensity factors using boundary elements has been done by a variety of methods, such as the extrapolation of displacements or stress, special crack tip elements, the subtraction of singularity technique, the strain energy release rate, and  $J$ -integral methods [9]. Techniques based on the extrapolation of displacements and stresses are easy to implement, but they require a very high level of mesh refinement in order to obtain accurate results. Alternating and virtual crack extension methods are also computationally expensive, as they require multiple computer runs to solve the problem. On the other hand, path-independent

integrals, being an energy approach, eliminate the need to solve local crack tip fields accurately, since if integration domains are defined over a relatively large portion of the mesh, an accurate modeling of the crack tip is unnecessary because the contribution to  $J$  of the crack tip fields is not significant. At the same time, the BEM is ideally suited for the evaluation of path-independent integrals, since the required stresses, strains, temperatures, and derivatives of displacements and temperatures can be directly obtained from their boundary integral representations. Using the BEM, Prasad et al. [7] implemented the  $J$ -integral due to Kishimoto et al. [10] for the analysis of two-dimensional thermoelastic problems. Its extension to three dimensions was presented by dell'Erba and Aliabadi [8] together with a decomposition method for the computation of the mixed mode stress intensity factors. Among the available methods for calculating fracture parameters, the energy domain integral (EDI) [11] has shown to be well-suited for three-dimensional BEM analysis. Applications of the EDI to solve three-dimensional crack problems using the BEM have been reported by Cisilino et al. for elasticity [12], elastoplasticity [13], and fiber-matrix interfaces in composite materials [14]. To develop the domain integral the EDI incorporates an auxiliary function  $\varphi$ , which can be interpreted as a virtual crack front advance. This makes the EDI similar to the virtual crack extension technique, but with the advantage that only one computer run is necessary to evaluate the pointwise energy release rate along the complete crack front. In a recent paper, Cisilino and Ortiz [15] combined the EDI with the  $M_I$ -integral methodology, for the analysis of mixed-mode cracks. In that work special emphasis was put on the selection of the auxiliary function  $\varphi$ . The function  $\varphi$  was found to be a key feature to obtain reliable results at the intersection of the crack front with free surfaces.

This work presents a BEM formulation of the EDI for the analysis of three-dimensional cracks in thermally stressed bodies. To the authors' knowledge this is the first time the EDI is used for the analysis of three-dimensional thermoelastic problems using the BEM. Following dell'Erba and Aliabadi [8] the thermoelastic problem is solved first by using the dual formulation of the BEM (the dual boundary element method or DBEM). The formulation of the EDI is presented in a straightforward approach, and the auxiliary function  $\varphi$  assimilated to a virtual crack-front extension. The computation of the EDI is implemented as a postprocessing technique, and so it can be applied to the results from a particular model at a later stage. The implementation takes advantage of the

<sup>1</sup>To whom correspondence should be addressed.

Contributed by the Applied Mechanics Division of ASME for publication in the JOURNAL OF APPLIED MECHANICS. Manuscript received June 7, 2005; final manuscript received December 21, 2005. Review conducted by R. M. McMeeking. Discussion on the paper should be addressed to the Editor, Prof. Robert M. McMeeking, Journal of Applied Mechanics, Department of Mechanical and Environmental Engineering, University of California–Santa Barbara, Santa Barbara, CA 93106-5070, and will be accepted until four months after final publication of the paper itself in the ASME JOURNAL OF APPLIED MECHANICS.

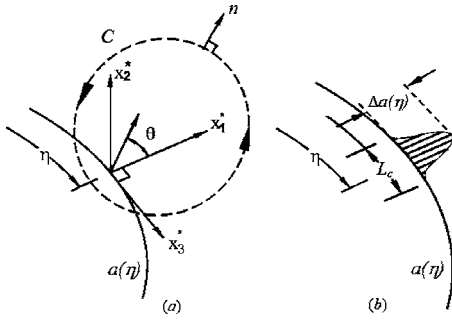


**Fig. 1 (a) Definition of the local orthogonal Cartesian coordinates at point  $\eta$  on the crack front. (b) Virtual crack front advance.**

efficiency of the boundary integral equations to directly obtain the required stresses, strains, temperatures, and displacement and temperature derivatives. Two approaches are studied for the selection of the auxiliary function  $\varphi$ , and their results compared and discussed. Several examples are analyzed to demonstrate the efficiency and accuracy of the implementation.

## 2 The Energy Domain Integral

Consider a three-dimensional crack front with a continuously turning tangent as depicted in Fig. 1(a). Define a local coordinate system  $x^*$  at position  $\eta$ , where the crack energy release rate is evaluated, given by  $x_1^*$  normal to the crack front,  $x_2^*$  normal to the crack plane, and  $x_3^*$  tangent to the crack front.

Following Natha and Moran [16], the energy release rate  $G(\eta)$  due to crack extension in its own plane along a three-dimensional crack front takes the form (see Fig. 1(a))

$$G(\eta) = \lim_{C \rightarrow 0} \xi_k(\eta) \int_{C(\eta)} (w \cdot \delta_{ki} - \sigma_{ij}^* u_{j,k}^*) n_i dC \quad (1)$$

where  $w$  is the strain energy density,  $\sigma_{ij}^*$  and  $u_{j,k}^*$  are Cartesian components of stress and displacement derivatives expressed in the local system  $x^*$ ,  $\xi_k(\eta)$  is the unit outward normal to the crack front in the local crack plane  $x_1^*$ - $x_3^*$ ,  $n_i$  is the unit vector normal to the contour  $C(\eta)$  (which lies in the  $x_1^*$ - $x_2^*$  plane), and  $dC$  is the differential of the arc length  $C$ . It is worth noting that, although Eq. (1) comes from a two-dimensional analysis, it applies for the three-dimensional case, as in the limit as  $C \rightarrow 0$ , plane strain conditions prevail so that three-dimensional fields approach to the plane problem.

Within the framework of uncoupled thermoelasticity, the strain is written as the sum of an elastic part  $\varepsilon_{ij}^e$  and a thermal part:

$$\varepsilon_{ij} = \varepsilon_{ij}^e + \alpha \theta \delta_{ij} \quad (2)$$

where  $\alpha$  is the coefficient of linear thermal expansion and  $\theta$  is temperature. If we make the additional restriction that thermal strains are bounded, a definition of  $w$  which can be used in Eq. (1) is:

$$w(\varepsilon_{ij}, \theta) = \int_0^{\varepsilon_{ij}^m} \sigma_{ij} \cdot d\varepsilon_{ij}^m \quad (3)$$

where  $\varepsilon_{ij}^m = \varepsilon_{ij} - \alpha \theta \delta_{ij}$  are the mechanical strains.

In order to derive the equivalent domain representation of Eq. (1), we consider a small segment  $L_c$  of the crack front that lies in the local  $x_1^*$ - $x_3^*$  plane as shown in Fig. 1(b). Next we assume that the segment undergoes a virtual crack advance in the plane of the crack, and we define the magnitude of the advance at each point  $\eta$  as  $\Delta a(\eta)$ . Note that  $\Delta a(\eta)$  varies continuously along  $L_c$  and it vanishes at each end of the segment. Now let

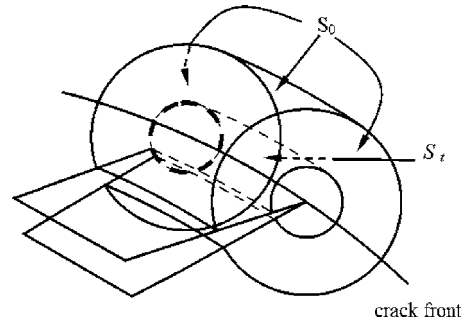


**Fig. 2 Tubular domain surrounding a segment of the crack front**

$$\bar{G}(\eta) = \int_{L_c} G(\eta) \Delta a(\eta) d\eta \quad (4)$$

where  $G(\eta)$  is the integral defined in Eq. (1). Note that while  $G(\eta)$  belongs to the point-wise energy release rate,  $\bar{G}$  gives the total energy released when the finite segment  $L_c$  undergoes the virtual crack advance.

The appropriate domain form of the point-wise crack-tip contour integral can be obtained from Eq. (1) by considering a tubular domain  $V$  surrounding the crack segment (see Fig. 2). As shown in the figure, the surface  $S_i$  is formed by translating the contour  $C$  along the segment  $L_c$ , and  $S_o$  stands for the outer surface of  $V$  including the ends. Next an auxiliary function  $\varphi$  is introduced, which is sufficiently smooth in  $V$  and it is defined on the surfaces of  $V$  as follows:

$$\varphi_k = \begin{cases} \Delta a(\eta) \cdot \xi_k(\eta) & \text{on } S_i \\ 0 & \text{on } S_o \end{cases} \quad (5)$$

Finally, in the limit as the tubular surface  $S_i$  is shrunk onto the crack segment  $L_c$ , and after applying the divergence theorem, the domain integral is obtained:

$$\bar{G} = \int_V \{[(\sigma_{ij}^* u_{j,k}^* - w \cdot \delta_{ki}) \varphi_{k,i} + \alpha \sigma_{ii}^* \theta_{,k} \varphi_k]\} dV \quad (6)$$

In the evaluation of the energy release rate, the integral given by Eq. (6) reduces to the domain representation of the familiar  $J$ -integral. A simple relationship between  $J(\eta)$  and  $\bar{G}$  can be obtained if it is assumed that  $\bar{G}$  is constant along the segment  $L_c$ . It follows directly from Eq. (4) that

$$J(\eta) = \frac{\bar{G}}{\int_{L_c} \Delta a(\eta) d\eta} \quad (7)$$

Finally, it is worth mentioning that the above derivation of the EDI assumes the absence of crack face tractions. If present, an extra term needs to be included in Eq. (6). For a more comprehensive derivation of the EDI the reader is referred to [11].

## 3 The Dual Boundary Element Method for Thermoelasticity

Consider a linear-elastic, isotropic and homogeneous body occupying a domain  $\Omega(X)$  enclosed by a boundary  $\Gamma(x)$  as illustrated in Fig. 3(a). The two governing equations for steady-state thermoelasticity are the Laplace and the Navier equations which can be written as follows:

$$\theta_{,kk} = 0 \quad (8)$$

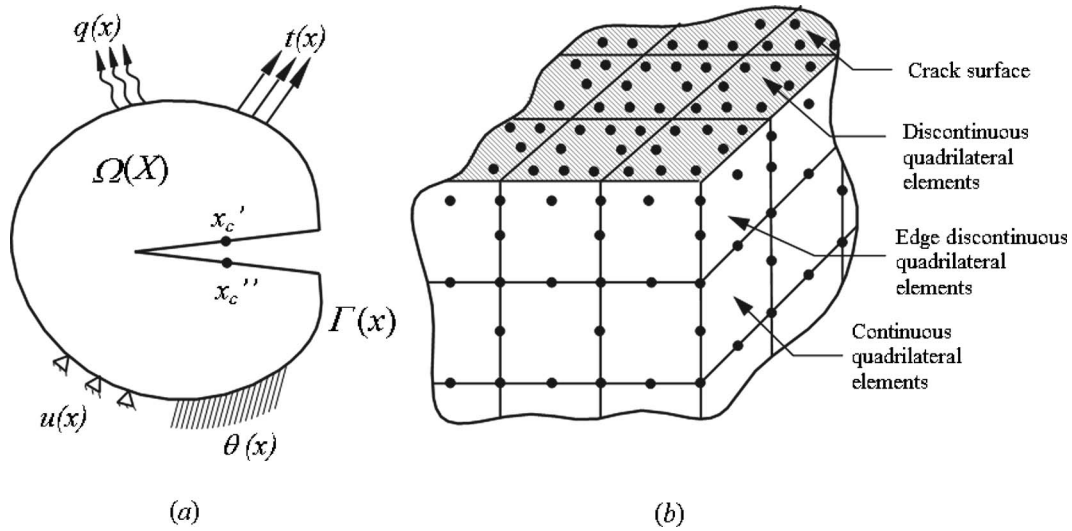


**Fig. 3 (a) General cracked body with mechanical and thermal boundary conditions. (b) Crack discretization strategy.**

$$\mu u_{i,jj} + \frac{\mu}{(1-2\nu)} u_{j,ij} - \frac{2\mu(1+\nu)}{(1-2\nu)} \alpha \theta_{,i} = 0 \quad (9)$$

where  $\theta$  is the temperature and  $u_i$  are the displacement components,  $\mu$  is the shear modulus,  $\nu$  is the Poisson's ratio, and  $\alpha$  is the coefficient of linear thermal expansion. Equations (8) and (9) are solved subject to boundary conditions in temperatures  $\theta$ , fluxes  $q$ , displacements  $u$ , and tractions  $t$  (see Fig. 3(a)).

The dual boundary integral equations on which the thermoelastic formulation of the DBEM is based are the temperature and the flux boundary integral equations for the solution of the Laplace equation, and the displacement and the traction integral equations for the solution of the Navier equation. The boundary integral temperature equation relating the boundary temperature  $\theta(x)$  with the boundary fluxes  $q(x)$  can be written as

$$c(x')\theta(x') - \int_{\Gamma} q^*(x',x)\theta(x)d\Gamma = - \int_{\Gamma} \theta^*(x',x)q(x)d\Gamma \quad (10)$$

where  $c(x')$  depends on the local geometry of the boundary surface at the position of point  $x'$ ;  $\theta^*(x',x)$  and  $q^*(x',x)$  are the temperature and flux fundamental solutions at a boundary point  $x$  due to a unit source placed at location  $x'$ . Expressions for the fundamental solutions  $\theta^*(x',x)$  and  $q^*(x',x)$  are given in the Appendix.

Assuming continuity of both temperatures and fluxes at  $x'$  on a smooth boundary, the boundary flux integral equation is obtained by differentiating Eq. (10):

$$c(x')q(x') - n_i(x') \oint_{\Gamma} \theta_i^{**}(x',x)q(x)d\Gamma = -n_i(x') \oint_{\Gamma} q_i^{**}(x',x)\theta(x)d\Gamma \quad (11)$$

where  $n_i(x')$  denotes the component of the outward unit normal to the boundary at  $x'$ . The symbols  $\oint$  and  $\oint$  represent integrals evaluated in the Cauchy and Hadamard principal value sense, respectively. Expressions for the kernels  $\theta_i^{**}(x',x)$  and  $q_i^{**}(x',x)$  are given in the Appendix.

If Eqs. (10) and (11) are used for collocation on coincident points on the crack surfaces (points  $x_c'$  and  $x_c''$  in Fig. 3(b)) the temperature and flux boundary integral equations can be written as

$$\frac{1}{2}\theta(x_c') + \frac{1}{2}\theta(x_c'') - \int_{\Gamma} q^*(x_c',x)\theta(x)d\Gamma = - \int_{\Gamma} \theta^*(x_c',x)q(x)d\Gamma \quad (12)$$

and

$$\begin{aligned} & \frac{1}{2}q(x_c'') - \frac{1}{2}q(x_c') - n_i(x_c'') \oint_{\Gamma} \theta_i^{**}(x_c'',x)q(x)d\Gamma \\ & = -n_i(x_c'') \oint_{\Gamma} q_i^{**}(x_c'',x)\theta(x)d\Gamma \end{aligned} \quad (13)$$

where the normal vectors  $n_i(x') = -n_i(x'')$  are assumed on the crack surface. At the same time it is also assumed that the crack surfaces at the position  $x_c'$  and  $x_c''$  are always smooth. The later assumption makes  $c(x') = 1/2$  in Eqs. (10) and (11).

Similarly to the boundary integral temperature equation, the displacement boundary integral equation relates the displacements  $u_j(x)$  with the boundary tractions  $t_j(x)$ , temperatures  $\theta(x)$ , and fluxes  $q(x)$ :

$$\begin{aligned} & c_{ij}(x')u_i(x') + \oint_{\Gamma} T_{ij}(x',x)u_j(x)d\Gamma - \int_{\Gamma} \bar{P}_i(x',x)\theta(x)d\Gamma \\ & = \int_{\Gamma} U_{ij}(x',x)t_j(x)d\Gamma - \int_{\Gamma} \bar{Q}_i(x',x)q(x)d\Gamma \end{aligned} \quad (14)$$

where  $U_{ij}(x',x)$  and  $T_{ij}(x',x)$  are the Kelvin traction and displacement fundamental solutions for elasticity, and  $\bar{P}_i(x',x)$  and  $\bar{Q}_i(x',x)$  are the fundamental fields that account for the thermal expansion (see the Appendix).

Assuming continuity of both strains and tractions at  $x'$  on a smooth boundary, the boundary traction integral equation is obtained by differentiating Eq. (14) and by applying the material constitutive relationships

$$\begin{aligned}
& \frac{1}{2}t_i(x') + n_j(x') \oint_{\Gamma} T_{kij}(x',x)u_k(x)d\Gamma - n_j(x') \oint_{\Gamma} \bar{P}_{ij}(x',x)\theta(x)d\Gamma \\
& + \frac{\mu(1+\nu)}{(1-2\nu)}\alpha n_i(x')\theta(x') \\
& = n_j(x') \oint_{\Gamma} U_{kij}(x',x)t_k(x)d\Gamma \\
& - n_j(x') \oint_{\Gamma} \bar{Q}_{ij}(x',x)q(x)d\Gamma \quad (15)
\end{aligned}$$

where the kernels  $T_{kij}(x'_c, x)$ ,  $U_{kij}(x'_c, x)$ ,  $\bar{P}_{ij}(x'_c, x)$ , and  $\bar{Q}_{ij}(x'_c, x)$  contain derivatives of the fundamental fields in Eq. (14) together with elastic constants.

If, as it has been done with their thermal counterparts, Eqs. (14) and (15) are used for collocation on coincident points on the crack surfaces, then the displacement and traction boundary integral equations can be written as

$$\begin{aligned}
& \frac{1}{2}u_i(x'_c) + \frac{1}{2}u_i(x''_c) + \oint_{\Gamma} T_{ij}(x',x)u_j(x)d\Gamma - \oint_{\Gamma} \bar{P}_{ij}(x',x)\theta(x)d\Gamma \\
& = \int_{\Gamma} U_{ij}(x',x)t_j(x)d\Gamma - \int_{\Gamma} \bar{Q}_{ij}(x',x)q(x)d\Gamma \quad (16)
\end{aligned}$$

and

$$\begin{aligned}
& \frac{1}{2}t_j(x''_c) - \frac{1}{2}t_j(x'_c) + n_j(x'_c) \\
& \oint_{\Gamma} T_{kij}(x'_c, x)u_k(x)d\Gamma - n_j(x''_c) \oint_{\Gamma} \bar{P}_{ij}(x'_c, x)\theta(x)d\Gamma \\
& + \frac{\mu(1+\nu)}{(1-2\nu)}\alpha n_i(x'_c)\theta(x'_c) \\
& = n_j(x'_c) \oint_{\Gamma} U_{kij}(x'_c, x)t_k(x)d\Gamma - n_j(x''_c) \oint_{\Gamma} \bar{Q}_{ij}(x'_c, x)q(x)d\Gamma \quad (17)
\end{aligned}$$

Following dell'Erba and Aliabadi [8], the general discretization strategy can be summarized as follows (see Fig. 3(b)):

- Crack surfaces are discretized using eight-node discontinuous quadrilateral elements in order to ensure the continuity requirements of the field variables for the existence of the flux and traction equations.
- Continuous elements are used over the remaining model boundary, except at the intersection of the crack with the boundary surface. Edge discontinuous elements are employed in this region in order to avoid common nodes at the intersection.
- The temperature integral equation (12) and the displacement integral equation (16) are applied for collocation on one of the crack surfaces.
- The flux integral equation (13) and the traction integral equation (17) are applied for collocation on the opposite crack surface.
- The temperature integral equation (10) and the displacement integral equation (14) are applied for collocation on all other surfaces.

## 4 Stresses, Strains, and Displacement and Temperature Derivatives

**4.1 Internal Points.** As it has been stated in Sec. 2, the computation of the EDI requires the stress, strain, and temperature

fields,  $\sigma_{ij}$ ,  $\varepsilon_{ij}$ , and  $\theta$ , and the displacement and temperature derivatives,  $u_{i,j}$  and  $\theta_{,k}$ , to be known within the integration volume  $V$ . Although these quantities must be expressed in the local crack-front coordinate system, in this work, and for the sake of simplicity, they are first computed in the global system and then transformed to the local crack-front coordinate system. Bearing this in mind, and in order to integrate the computation of the EDI into the DBEM formulation, derivatives of the displacements at internal points  $X'$  are obtained from their boundary integral representations. Thus, the integral equations for the displacement and temperature derivatives result from the analytical differentiation of the internal counterparts of Eqs. (10) and (14):

$$\theta_{,k}(X') = \int_{\Gamma} q_{,k}^{**}(X',x)\theta(x)d\Gamma - \int_{\Gamma} \theta_{,k}^{**}(X',x)q(x)d\Gamma \quad (18)$$

and

$$\begin{aligned}
u_{i,k}(X') = & - \int_{\Gamma} T_{ij,k}(X',x)u_j(x)d\Gamma + \int_{\Gamma} \bar{P}_{i,k}(X',x)\theta(x)d\Gamma \\
& + \int_{\Gamma} U_{ij,k}(X',x)t_j(x)d\Gamma - \int_{\Gamma} \bar{Q}_{i,k}(X',x)q(x)d\Gamma \quad (19)
\end{aligned}$$

where the kernels  $q_{,k}^{**}(X',x)$ ,  $\theta_{,k}^{**}(X',x)$ ,  $T_{ij,k}(X',x)$ ,  $U_{ij,k}(X',x)$ ,  $\bar{P}_{i,k}(X',x)$ , and  $\bar{Q}_{i,k}(X',x)$  are the derivatives of the fundamental solutions.

Once the displacement derivatives  $u_{j,k}$  are known, stresses  $\sigma_{ij}$  and strains  $\varepsilon_{ij}$  are computed using basic continuum mechanics relationships:

$$\varepsilon_{ij} = \frac{1}{2}(u_{i,j} + u_{j,i}) + \alpha\theta\delta_{ij} \quad (20)$$

$$\sigma_{ij} = \frac{E}{1+\nu} \left( \varepsilon_{ij} + \frac{\nu}{1-2\nu} \varepsilon_{kk} \delta_{ij} \right) - \frac{E}{1-2\nu} \alpha\theta\delta_{ij} \quad (21)$$

**4.2 Boundary Points.** Temperature and displacement derivatives  $\theta_{,k}$  and  $u_{i,j}$  at boundary nodes could be obtained from Eqs. (18) and (19) in a similar way to their internal counterparts, by taking the limit of Eqs. (18) and (19) as point  $X'$  moves to the boundary, i.e.,  $X' \rightarrow x'$ . However, this procedure is computationally expensive because of the occurrence of hypersingular integrands. To avoid this difficulty, stresses and strains, as well as the displacements and temperatures on the model surface, are evaluated in this work from the boundary displacements, tractions, temperatures, and fluxes following a procedure similar to that used in FEM computations. Consider with this purpose a local Cartesian system,  $(x_1^0, x_2^0, x_3^0)$ , such that  $x_3^0$  is the unit vector in the normal direction to the boundary element and  $x_1^0$  and  $x_2^0$  are unit vectors which define the local tangential plane. If  $\sigma_{ij}^0$  and  $t_i^0$  are stresses and tractions in the local system, stress components in the normal direction can be written as

$$\sigma_{i3}^0 = t_i^0 \quad (22)$$

The remaining stress tensor components,  $\sigma_{11}^0$ ,  $\sigma_{12}^0$ , and  $\sigma_{22}^0$  can be expressed in terms of  $t_3^0$  and the tangential strain tensor components  $\varepsilon_{11}^0$ ,  $\varepsilon_{12}^0$ , and  $\varepsilon_{22}^0$ , by eliminating  $\varepsilon_{33}^0$  from the general expression of Hooke's law. Thus,

$$\sigma_{11}^0 = \frac{1}{1-\nu} [\nu t_3^0 + 2\mu(\varepsilon_{11}^0 + \nu\varepsilon_{22}^0) - (1+\nu)\alpha\theta]$$

$$\sigma_{22}^0 = \frac{1}{1-\nu} [\nu t_3^0 + 2\mu(\varepsilon_{22}^0 + \nu\varepsilon_{11}^0) - (1+\nu)\alpha\theta]$$

$$\sigma_{12}^0 = 2\mu\varepsilon_{12}^0 \quad (23)$$

Strain components  $\varepsilon_{ij}^0$  can be obtained using Eq. (20), now applied in the local coordinate system. It is worth nothing that displace-



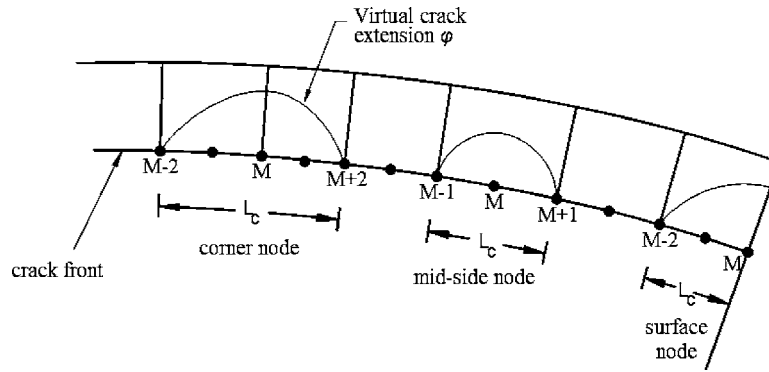


**Fig. 4 Schematic of the volume cells in the crack front region illustrating the virtual crack extensions for a corner node, a mid-node, and a surface node**

ment derivatives in Eq. (20) are initially evaluated in the intrinsic element directions  $(\xi_1, \xi_2)$  and then converted to the local coordinate system  $x^0$  since, as usual in the BEM, boundary displacements are approximated in terms of the piecewise parametric representation (shape functions) of intrinsic coordinates:

$$u_i(\xi_1, \xi_2) = \sum_{n=1}^8 \Phi^n(\xi_1, \xi_2) u_i^n \quad (24)$$

where  $\Phi^n$  are the shape functions and  $u_i^n$  are the nodal values of the displacements.

From (24) it follows

$$\frac{\partial u_i}{\partial \xi_j} = \sum_{n=1}^8 \frac{\partial \Phi^n}{\partial \xi_j} u_i^n \quad (25)$$

Finally, the derivatives of the displacements in the global system are computed. Using chain differentiation, derivatives of the displacements in the global system,  $u_{i,m}$ , can be related to the derivatives of the displacements in the intrinsic boundary element directions,  $\partial u_i / \partial \xi_j$ , as follows:

$$\frac{\partial u_i}{\partial \xi_j} = \frac{\partial u_i}{\partial x_m} \frac{\partial x_m}{\partial \xi_j} \quad (26)$$

where  $\partial x_m / \partial \xi_j$  is the Jacobian matrix of the transformation. The nine components of the displacement derivatives  $u_{i,m}$  can be retrieved by solving for each case a system of equations constructed using expressions (26). For further details the reader is referred to the works by Cisilino et al. [12,13,15].

A similar procedure can be employed for the computation of the temperature derivatives on the model boundary.

## 5 Boundary Element Implementation

**5.1 Energy Domain Integral Evaluation.** As it has been stated in Sec. 2, Eq. (6) allows computation of the  $J$ -integral at any position  $\eta$  on the crack front. This requires the evaluation of a volume integral within domains that enclose a segment of the crack front  $L_c$ . A natural choice here is to make  $\eta$  coincident with the element nodes on the crack front, while  $L_c$  is taken as the element or element sides at which points  $\eta$  lies (see Fig. 4).

The portion of the model domain in which the volume integrals are evaluated is discretized using 20-node isoparametric (brick) cells, over which stresses, strains, and displacements and temperature derivatives are approximated by products of the cell interpolation functions,  $\psi^n$ , and the nodal values of  $\sigma_{ij}$ ,  $\varepsilon_{ij}$ ,  $u_{ij}$ , and  $\theta_k$ . Nodal values of these variables are computed following the procedures introduced in Secs. 4.1 and 4.2 depending on whether the node is internal or it lies on the model boundary. Volume discretization is designed to have a web-style geometry around the crack

front, while the integration volumes are taken coincident with different rings of cells. This is illustrated for an example in Fig. 5, where one of the model faces has been removed to show the crack and the integration domains.

As depicted in Fig. 4, three different cases need to be considered, depending on whether the node of interest  $M$  is in the middle of an element side (mid-node), it is shared by two elements (cor-

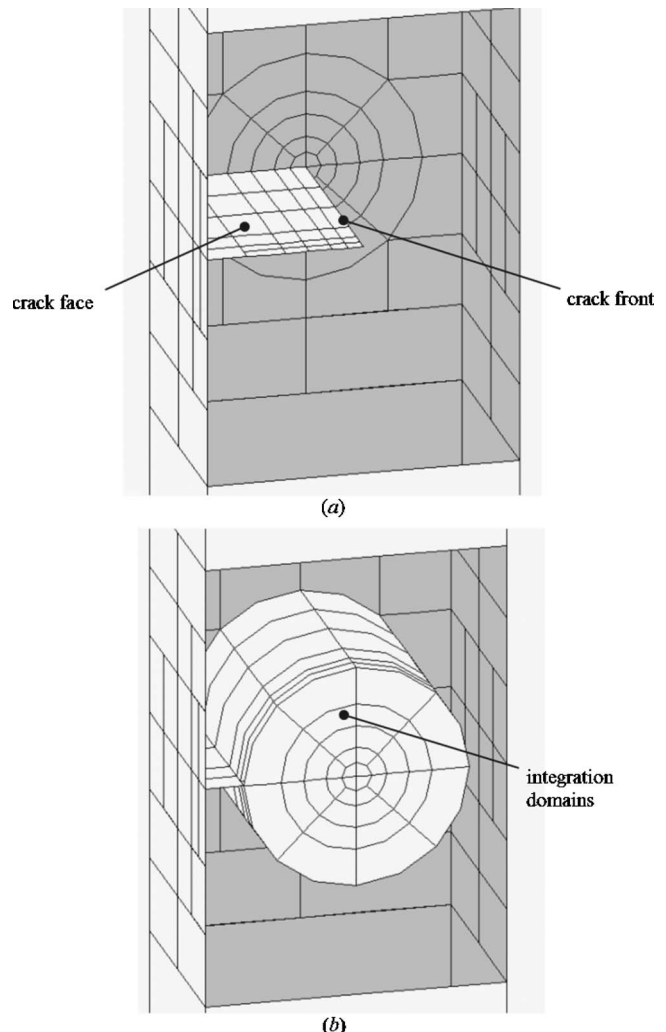


**Fig. 5 Boundary element discretization and integration cells**

ner node), or it is located coincident with the external surface (surface node). If the node  $M$  is a mid-node or surface node,  $L_c$  (the segment of the crack front over which the  $J$ -integral is computed) spans over one element, connecting nodes  $M-1$ ,  $M$ , and  $M+1$  and nodes  $M-2$ ,  $M-1$ , and  $M$ , respectively. On the other hand, if  $M$  is a corner node,  $L_c$  spans over two elements, connecting nodes from  $M-2$  to  $M+2$ .

The function  $\varphi$  is used to specify the virtual crack extension. For the sake of simplicity the direction of the crack extension is taken constant along  $L_c$  and coincident with the three orthogonal local directions defined at  $\eta$  (see Fig. 1(a)). Consistent with the isoparametric formulation,  $\varphi$  is given by

$$\varphi_k = \sum_{i=1}^{20} \Psi^i \varphi_k^i \quad (27)$$

where  $\Psi^i$  are the cell interpolation functions and  $\varphi_k^i$  are the nodal values for the  $i$ th node. From the definition of  $\varphi$  (see Eq. (5)),  $\varphi_k^i = 0$  if the  $i$ th node is on  $S_0$  (the outer surface of the integration domain) and  $\varphi_k^i \neq 0$  for the nodes on  $L_c$ . In particular  $\varphi_k^i = 1$  for the node at  $\eta$  (nodes labeled  $M$  in Fig. 4). Different criteria for specifying  $\varphi_k^i$  for the other nodes  $L_c$  and for the nodes inside the integration domain  $V$  are discussed in next section.

Following standard manipulations

$$\varphi_{k,j} = \sum_{i=1}^{20} \sum_{n=1}^3 \frac{\partial \Psi^i}{\partial \xi_n} \frac{\partial \xi_n}{\partial x_j} \varphi_k^i \quad (28)$$

where  $\xi_n$  are the coordinates in the cell isoparametric space.

If Gaussian integration is used, the discretized form of Eq. (6) is given by

$$G = \sum_{\text{cells in } V} \sum_{p=1}^m \left[ [(\sigma_{ij}^* \mu_{j,k}^* - w \cdot \delta_{ki}) \varphi_{k,i} + \alpha \sigma_{ii}^* \theta_{k,k} \varphi_k] \det \left( \frac{\partial x_i}{\partial \xi_k} \right) \right] w_p \quad (29)$$

where  $m$  is the number of Gaussian points per cell and  $w_p$  are the weighting factors.

**5.2 The  $\varphi$ -Function.** Since the virtual crack advance can adopt any arbitrary shape, the only requirement for the function  $\varphi$  is to be sufficiently smooth within the integration volume  $V$  as the evaluation of the EDI requires of its differentiation. Although Shih et al. [11] have shown that the EDI is insensitive to the assumed shape of the  $\varphi$  function, it has been found in a recent work by one of the authors of this paper [15] that the shape of the function  $\varphi$  could be relevant for the performance of the EDI computations. In this sense two different approaches for the shape of the function  $\varphi$  are investigated.

**5.2.1 Bi-quadratic  $\varphi$ .** The bi-quadratic definition of  $\varphi$  has been employed with excellent results in the computation of EDI in previous works by Cisilino et al. [12–14]. Within this approach  $\varphi$  is defined to vary quadratically in the directions tangential and normal to the crack front. Considering that  $\eta$  is at the middle of the crack front segment  $L_c$ , and that  $r_0$  is the radius of the integration domain, the function  $\varphi$  is written as:

$$\varphi(x) = \left\| 1 - \left( \frac{x_3}{L_c/2} \right)^2 \right\| \cdot \left[ 1 - \left( \frac{r}{r_0} \right)^2 \right] \quad (30)$$

where  $r$  is the distance from the crack front in the  $x_1^*-x_2^*$  plane as depicted in Fig. 1.

**5.2.2 Optimized  $\varphi$ .** Saliva et al. [17] proposed an optimum shape for the function  $\varphi$ , which under certain considerations ensures the convergence of the EDI computations. The proposed function is

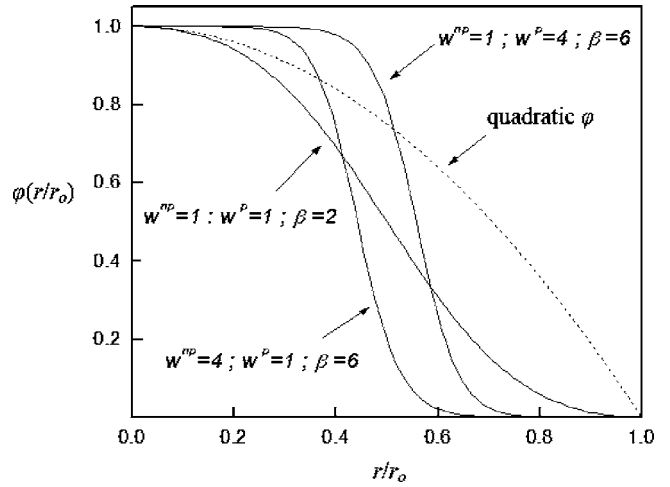


**Fig. 6 Influence of parameters  $w^p$ ,  $w^{np}$ , and  $\beta$  on the shape of function  $\varphi$  (one-dimensional case)**

$$\varphi(x) = \frac{w^p \|x\|^{-\beta}}{w^p \|x\|^{-\beta} + \sum_{i=1}^N w_j^{np} \|x - z_i\|^{-\beta}} \quad (31)$$

where  $w^p$ ,  $w^{np}$ , and  $\beta$  are parameters to be chosen, and  $z_i$  are the positions of the  $N$  points with null prescribed values of  $\varphi$ . These are given in this work by the  $N$  cell-nodes located on  $S_0$ , the outer surface of the integration volume  $V$ .

Using parameters  $w^p$ ,  $w^{np}$ , and  $\beta$ , it is possible to control the shape of  $\varphi$  and consequently the parts of the domain with the most significant contribution to the integral in Eq. (6). In particular  $\beta$  is associated with the smoothness of  $\varphi$ . Greater values induce approximately null gradients around the crack front, where non-null values of  $\varphi$  are prescribed. In contrast, the field undergoes abrupt changes outside these regions. With  $w^p$  and  $w^{np}$ , the region with non-null gradients can be translated near the crack front or near the boundary of the integration volume where null values of  $\varphi$  are prescribed. Figure 6 illustrates the influence of the parameters as a function of the normalized distance  $r/r_0$ .

It is important to mention here that the previous works which made use of the optimized  $\varphi$ , Refs. [15,17], were devoted to the solution of linear elastic crack problems without the presence of body loads. Under these circumstances, the second term of the integral in Eq. (6), the term which accounts for body loads (thermal loads in our case), vanishes. The key feature for the excellent performance of the optimized  $\varphi$  for problems without body loads can be attributed to the behavior of  $\varphi$  in the crack tip vicinity. Note that for the optimized definition of  $\varphi$ , the gradient  $\varphi_{,i}$  is zero in the vicinity of the crack front (see Fig. 6), resulting in that the contribution to  $G$  of the crack front fields is not significant. As a consequence, the zone of the integration domain with the lowest accuracy in the results has a marginal contribution to the value of  $G$ .

The formulation of the EDI for thermoelastic problems includes a term to account for the thermal loads (see Eq. (6)). Note that since this term is multiplied by  $\varphi$ , the justification given in the previous paragraph for the excellent performance of the optimized  $\varphi$  is not longer valid. However, and as it will be shown in the following sections, the shape of  $\varphi$  still contributes to the accuracy of the EDI computations.

## 6 Examples

**6.1 Edge Crack in a Thin Panel Subjected to a Linear Thermal Field.** An example with two-dimensional characteristics is proposed for the first example. It consists of an edge-cracked

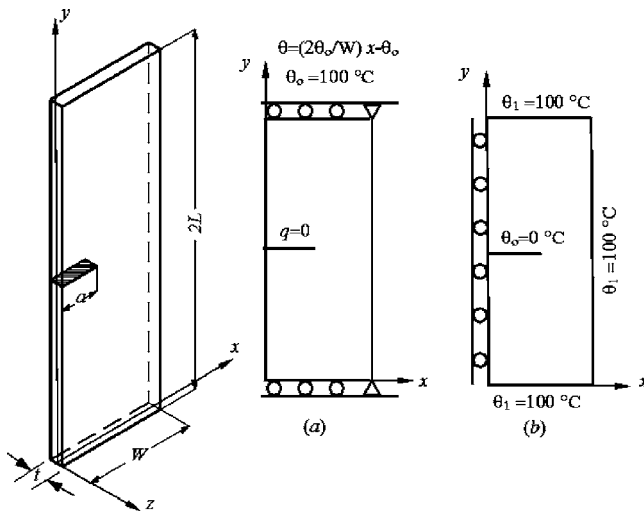


**Fig. 7 Geometry, dimensions, and boundary conditions for the edge and center cracked specimens**

thin panel illustrated in Fig. 7(a). The crack length is  $a=10$  mm, and the specimen dimensions  $W=2a$ ,  $L=W$ , and  $t=a/10$ . Material properties are Young modulus  $E=1000$  N/mm<sup>2</sup>, Poisson ratio  $\nu=0.3$ , coefficient of thermal expansion  $\alpha=10^{-5}/^{\circ}\text{C}$ , and thermal conductivity  $\lambda=1$  W/ $^{\circ}\text{C}\cdot\text{mm}$ . The specimen is subjected to a linear temperature variation throughout the width  $W$ , with zero temperature at mid-width, and temperatures  $\theta_0=\pm 100^{\circ}\text{C}$  at the right and left edges, respectively (see Fig. 7(a)). Crack surfaces are isolated. Displacement boundary conditions at the panel ends are illustrated in Fig. 7(a). Lateral faces of the specimen ( $z=\pm t/2$ ) are isolated and their normal displacements are restricted in order to simulate the plane strain condition.

Model discretization follows the same pattern of that illustrated in Fig. 5, but with only one element in the direction of the specimen thickness. Two meshes are considered: a “coarse” mesh consisting of 242 elements and 899 nodes, and a “fine” mesh consisting of 374 elements and 1319 nodes. Seven rings of internal cells with radii ranging from 5% to 75% of the crack length are constructed around the crack tip for the  $J$  computations. For the so-called coarse mesh, 60 cells and 526 nodes are used. On the other hand, 116 cells and 958 nodes are used for the fine mesh. The bi-quadratic definition of the function  $\varphi$  is used for the solution of this problem.

Obtained results for the two discretizations are reported in Tables 1 and 2 in terms of normalized mode-I stress intensity

factor  $K_I^*$ . Stress intensity factors were computed from  $J$  results via the well-known expression  $K_I=\sqrt{J\cdot E/(1-\nu^2)}$  and later normalized using  $K_I^*=K_I/\sigma_{\theta}\sqrt{\pi a}$ . The symbol  $\sigma_{\theta}=\alpha E\theta_0/(1-\nu)$  stands for the exact solution for the thermal stress in the  $y$ -direction at the right edge of an uncracked specimen. Results are reported for crack front points located on the specimen surface and on its mid-plane, and they are compared to the solution reported by Wilson and Yu [18] who solved the problem using finite elements. Differences between computed results and the reference solution are denoted as  $\Delta\%$ .

Tables 1 and 2 show the improvement of the results with the refinement of the model discretization. While for the coarse mesh the differences between the computed results and the reference value are close to 5%, they drop to less than 1% for the fine mesh. The only exception is the results obtained for the smallest integration domain ( $r/a=0.05$ ) which is defined using only one ring of cells. It is also worth noting the excellent agreement between the interior and surface values and the independence of the results with the integration path. The overall performance of the implemented algorithm is found to be very good, with an accuracy level similar to other applications of the EDI [12–14]. As usual when dealing with  $J$ -integral computations, the most accurate results are obtained for integration paths defined over a relatively large portion of the mesh.

**6.2 Thin Panel With a Central Crack Subjected to a Thermal Field.** The second example consists in a center-cracked thin panel in plane strain condition. The model geometry is the same of the first example, but with the addition of the symmetry conditions (both thermal and displacement) at  $x=0$  (see Fig. 7(b)). The thermal field is given as follows: temperature for crack surfaces are  $\theta_0=0^{\circ}\text{C}$  while the temperatures for all the surfaces perpendicular to the  $x$ - $y$  plane ( $x=W$ ,  $y=0$  and  $y=2L$ ) are  $\theta_1=100^{\circ}\text{C}$ . As in the previous example, the lateral faces of the model are isolated and their normal displacements restricted in order to simulate the plane strain condition.

Normalized stress intensity factor results  $K_I^*=K_I/\alpha E(\theta_1-\theta_0)\sqrt{W}$  are reported in Table 3 and compared to those reported by Murikami et al. [1]. All results were computed using the fine discretization and the bi-quadratic  $\varphi$ . As in the previous example  $K$  results are reported for crack front points located on the specimen surface and on the mid-plane. Excellent agreement is obtained between the computed and the reference results, with a difference less than 2% for all the integration domains.

**6.3 Penny-Shaped Crack in a Cylindrical Bar Subjected to a Thermal Field.** A bar of circular cross section containing an embedded penny-shaped crack is analyzed in this example (see

**Table 1 Normalized  $K$  results  $K_I^*=K_I/\sigma_{\theta}\sqrt{\pi a}$  for the edge crack in a thin panel (coarse discretization)**

	$r/a$							Average	Ref. [18]
	0.05	0.09	0.15	0.225	0.338	0.50	0.75		
Surface	0.534	0.527	0.525	0.525	0.526	0.528	0.529	0.528	0.504
$\Delta\%$	5.95	4.56	4.17	4.17	4.37	4.76	4.96	4.71	...
Interior	0.538	0.529	0.527	0.526	0.528	0.53	0.532	0.530	0.504
$\Delta\%$	6.75	4.96	4.56	4.37	4.76	5.16	5.56	5.16	...

**Table 2 Normalized  $K$  results  $K_I^*=K_I/\sigma_{\theta}\sqrt{\pi a}$  for the edge crack in a thin panel (fine discretization)**

	$r/a$							Average	Ref. [18]
	0.05	0.09	0.15	0.225	0.338	0.50	0.75		
Surface	0.482	0.497	0.501	0.501	0.502	0.502	0.502	0.498	0.504
$\Delta\%$	-4.37	-1.39	-0.60	-0.60	-0.40	-0.40	-0.40	-1.16	...
Interior	0.489	0.5	0.502	0.502	0.503	0.503	0.503	0.500	0.504
$\Delta\%$	-2.98	-0.79	-0.40	-0.40	-0.20	-0.20	-0.20	-0.74	...

**Table 3 Normalized  $K$  results  $K_I^* = K_I / \alpha E (\theta_1 - \theta_0) \sqrt{W}$  for the edge crack in a thin panel (coarse discretization)**

	$r/a$							Average	Ref. [1]
Surface	0.05	0.09	0.15	0.225	0.338	0.50	0.75	0.490	0.495
$\Delta\%$	0.497	0.489	0.487	0.486	0.486	0.486	0.496	-1.10	...
Interior	0.40	-1.21	-1.62	-1.82	-1.82	-1.82	0.20	0.490	0.495
$\Delta\%$	0.497	0.489	0.487	0.486	0.486	0.486	0.496	-1.10	...
$\Delta\%$	0.40	-1.21	-1.62	-1.82	-1.82	-1.82	0.20	-1.10	...

Fig. 8(a)). The crack of radius  $a=1$  mm is located in the center of the bar, in a plane perpendicular to the axis of the bar. In order to assimilate the problem to that of a penny-shaped crack embedded in an infinite body, the dimensions  $R/a=10$  and  $H/R=6$  are chosen. The temperature of the crack surfaces is set  $\theta_0=0^\circ\text{C}$  while for all the surfaces of the cylinder  $\theta_1=100^\circ\text{C}$ . The boundary element mesh consists of 1434 nodes and 224 elements. The crack is discretized using 152 elements. Three rings of cells with radii  $r/a=0.2, 0.35$ , and  $0.50$  are used for the  $J$  computations. With this purpose 832 cells are employed. Material properties are adopted the same as the previous examples. The bar is allowed to expand freely.

Normalized  $K$  results  $K_I^* = K_I / (\alpha E \theta_0 \sqrt{a\pi} / (1-\nu))$  calculated along the crack front using the bi-quadratic  $\varphi$  are reported in Table 4. Also included in Table 4 is the analytical solution due to Das [19] for comparison. Since the  $K$  result is constant along the crack front, results in Table 4 are reported only for a few positions. Table 4 shows that the EDI results deviate less than 3% from the reference solution, which is considered acceptable for the mesh used. No attempt was made to refine the mesh.

**6.4 Circular Bar With an Annular Crack Subjected to a Thermal Field.** The problem of an annular crack in a circular bar is considered in this example (see Fig. 8(b)). The crack is situated at the bar mid-length, on a plane perpendicular to its axis. Model dimensions are crack depth  $a=20$  mm, cylinder radius  $R/a=2.5$ , and cylinder height  $H/R=12$ . The thermal field is given by temperatures  $\theta_0=-50^\circ\text{C}$  on the crack surfaces and  $\theta_1=0^\circ\text{C}$  on the top and the bottom ends of the cylinder. The lateral surface of the cylinder is isolated. The boundary element discretization consists of 1970 nodes and 328 elements, 192 of which are used for the crack faces. Three rings of cells with radii  $r/a=0.2, 0.35$ , and  $0.50$  are used for the  $J$  computations. Axial displacements are restricted for the top and bottom ends of the cylinder.

The picture in Fig. 8(c) illustrates boundary element mesh in

the deformed configuration. Some of the elements in the lateral surface of the cylinder have been removed in order to see the crack discretization. Obtained results using the bi-quadratic  $\varphi$  are presented in Table 5 in terms of the normalized stress intensity factors  $K_I^* = K_I / (\alpha E \theta_0 \sqrt{a\pi})$  for a number of positions along the crack front. Although there is not reference solution available for comparison, the independence of the results with the integration path can be verified. Thus, the last column in Table 5 reports the maximum deviation of the results with respect to the average value. Maximum deviation is always less than 1%.

**6.5 Edge Crack in a Thick Panel Subjected to a Linear Thermal Field.** This example consists of a problem with three-dimensional characteristics for which the variation of  $J$  along the crack front is studied. The problem loading and geometry are the same as that of the example studied in Sec. 6.1, but considering now a panel of length  $2L=6W$  and thickness  $t=3a$ . Since the problem is symmetric with respect to the plane  $z=-t/2$  (see Fig. 7(a)), only one half of its geometry is modeled. The devised boundary element discretization consists of 292 elements and 1351 nodes. Six elements are placed along the crack front and a total of 35 elements are used in the crack discretization. Crack front elements are graded towards the free surface, the smallest one being equal to  $t/32$  (see Fig. 5). Four rings of cells with radii  $r/a=0.2, 0.35, 0.5$ , and  $0.75$  are accommodated around the crack front for  $J$  computations. With this purpose 480 cells and 2302 nodes are employed.

$J$ -integral values are computed using the two approaches introduced in Sec. 5 for the specification of  $\varphi$ . Afterwards,  $K$ -values are calculated from  $J$  results using  $K_I = \sqrt{J \cdot E / (1-\nu^2)}$ , and later normalized by doing  $K_I^* = K_I / \alpha E \theta_0 \sqrt{W}$ . Results for the bi-quadratic definition of  $\varphi$  are plotted in Fig. 9(a), while results obtained using optimized  $\varphi$  are plotted in Fig. 9(b). Following Ortiz and Cisilino [14] the values of the parameters for the opti-

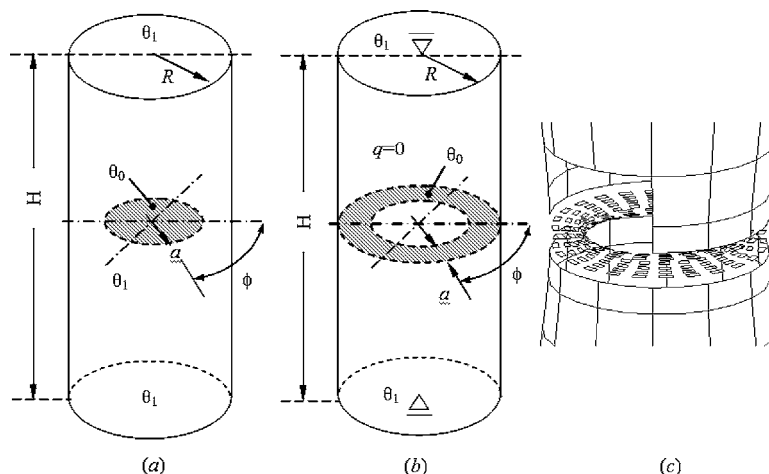


**Fig. 8 Geometry, dimensions, crack discretization, and boundary conditions for the penny-shaped and annular cracks**



**Table 4 Normalized  $K$  results  $K_I^* = K_I / (\alpha E \theta_0 \sqrt{a/\pi(1-\nu)})$  for the penny-shaped crack in a cylindrical bar**

$\phi/2\pi$	$r/a$			Average	Ref. [19]	$\Delta\%$
	0.20	0.35	0.50			
0.000	0.9580	0.9730	0.9779	0.9696	0.9418	2.95
0.125	0.9573	0.9720	0.9762	0.9685	0.9418	2.83
0.250	0.9575	0.9721	0.9764	0.9687	0.9418	2.85
0.375	0.9575	0.9720	0.9763	0.9686	0.9418	2.84
0.500	0.9576	0.9722	0.9764	0.9687	0.9418	2.86
0.625	0.9577	0.9722	0.9764	0.9688	0.9418	2.86
0.750	0.9576	0.9721	0.9764	0.9687	0.9418	2.85
0.875	0.9576	0.9721	0.9764	0.9687	0.9418	2.85

mized  $\varphi$  are chosen as  $w^p=6$ ,  $w^{np}=1$ , and  $\beta=6$ . Error bars in the plots indicate the maximum deviation for the results obtained using the different integration domains. Reference values in the plots are those reported by dell'Erba et al. [8] using COD computations from BEM results. In the region near the symmetry plane,  $z/t=0$ , a plane strain condition is expected, and thus the result by Wilson and Yu [18] for two-dimensional analysis is also included for comparison.

Both approaches for  $\varphi$  provide results within a 4% error with respect to the plane strain solution at the position of the symmetry plane,  $z/t=0$ . For positions along the crack front located in the interior of the specimen, results computed using the bi-quadratic  $\varphi$  show a more stable and robust behavior than those obtained using the optimized  $\varphi$ . On the other hand, the optimized  $\varphi$  results are more reliable for the computations in the region of the crack front near to the free surface. Note that in such a case  $K$  values computed using the optimized  $\varphi$  are almost independent of the integration domains, while those computed using the optimized  $\varphi$  exhibit a relatively large dispersion. Finally, it is worth mentioning that results obtained using both approaches for  $\varphi$  are always higher than those reported by dell'Erba et al. [8] and closer to the plane strain solution. Both sets of results, those computed in this work and those reported by dell'Erba et al. [8], tend to the same value at the free surface.

**6.6 Thick Panel With a Central Crack Subjected to Thermal Field.** The last example consists of a thick panel with a central crack. Model geometry and boundary conditions are the same as that illustrated in Fig. 8(b) and used in the example in Sec. 6.2, but with the specimen the thickness increased to  $t=3a$ . Following the previous example, the  $J$ -integral and their corresponding  $K$ -values are computed along the crack front. Model discretization is the same as used in the previous example. Appropriate displacement boundary conditions are set in order to account for the symmetry conditions.

Normalized  $K$ -results  $K_I^* = K_I / (\alpha E (\theta_1 - \theta_0) \sqrt{W})$  are reported in Figs. 10(a) and 10(b) for the bi-quadratic and optimized  $\varphi$ , respectively. Parameters for the optimized  $\varphi$  are chosen as  $w^p=6$ ,

**Table 5 Normalized  $K$  results  $K_I^* = K_I / (\alpha E \theta_0 \sqrt{a/\pi})$  for the penny-shaped crack in a cylindrical bar**

$\phi/2\pi$	$r/a$	Average	Maximum deviation %		
	0.20	0.35	0.50		
0,000	0,164	0,166	0,166	0,166	0,618
0,104	0,166	0,168	0,168	0,167	0,605
0,208	0,165	0,167	0,167	0,166	0,872
0,313	0,166	0,168	0,168	0,167	0,604
0,417	0,165	0,167	0,167	0,166	0,872
0,521	0,166	0,168	0,168	0,167	0,605
0,625	0,165	0,167	0,167	0,166	0,872
0,729	0,166	0,168	0,168	0,167	0,605
0,833	0,165	0,167	0,167	0,166	0,872
0,938	0,166	0,168	0,168	0,167	0,604

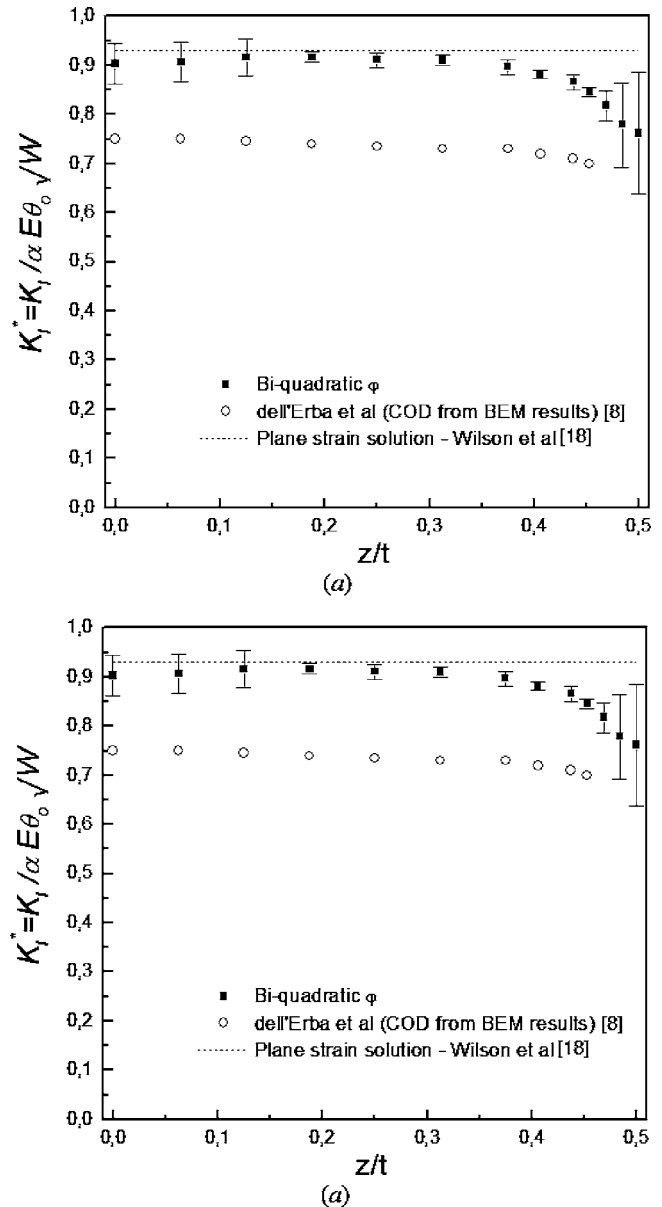


**Fig. 9 Normalized mode I stress intensity factor along the crack front for the edge crack in a thick panel: (a) results using bi-quadratic  $\varphi$  and (b) results using optimized  $\varphi$**

$w^{np}=1$ , and  $\beta=6$ . As for the previous example, error bars indicate the maximum deviation in the results with respect to the integration domains.

Computed results show the same general behavior of the previous example: both approaches for  $\varphi$  provide results very close to the plane strain solution for the symmetry plane (position  $z/t=0$ ), the bi-quadratic  $\varphi$  behaves more stable and robust than the optimized  $\varphi$  in the interior of the specimen, and the optimized  $\varphi$  results are more appropriate for the computations on the free surface. At this point it is worth noting that although both approaches result in the same  $K$ -value at the free surface (see Fig. 10), those computed using the bi-quadratic  $\varphi$  possess nearly 20% dispersion, while for the optimized  $\varphi$  the dispersion is only 3%.

## 7 Conclusions

A three-dimensional dual boundary element method formulation of the energy domain integral for the numerical analysis of thermoelastic fracture problems has been presented in this paper.

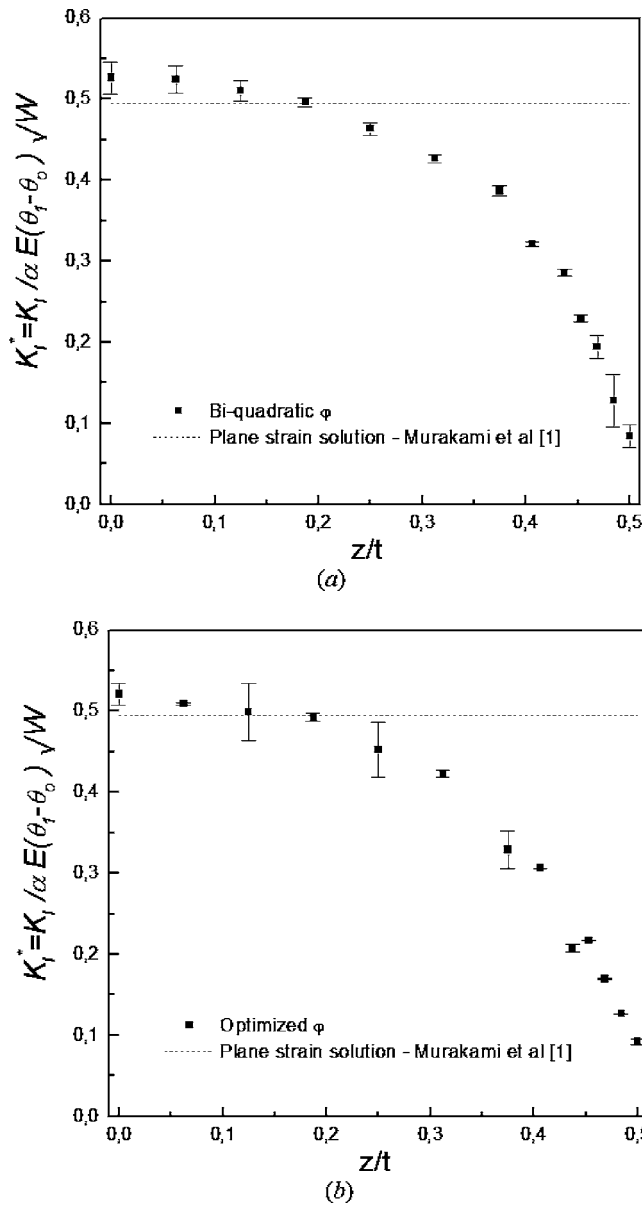


**Fig. 10 Normalized mode I stress intensity factor along the crack front for the central crack in a thick panel: (a) results using bi-quadratic  $\varphi$  and (b) results using optimized  $\varphi$**

The proposed formulation has been implemented as a post-processing technique, and so it can be applied to the results from a particular model at a later stage. The implementation takes advantage of the efficiency of the boundary integral equations to directly obtain the required stress, strains, temperatures, and displacement and temperature derivatives. A number of examples have been solved to demonstrate the efficiency and accuracy of the proposed formulation. Obtained results are accurate and in good agreement with other results reported in the literature.

Special emphasis has been put on the appropriate selection of the auxiliary function  $\varphi$  present in the domain integral formulation. In this sense two approaches have been considered: a bi-quadratic variation and an optimized approach proposed in the paper by Saliva et al. [17].

It has been found that the function  $\varphi$  constitutes a key feature for the performance of the proposed methodology. Obtained results show that the optimized  $\varphi$  performs markedly better for the point located at the intersection of the crack front with the free surface, allowing obtaining reliable  $J$  results where the bi-

quadratic  $\varphi$  fails. On the other hand, for crack front positions located in the interior of the specimen both approaches allow computing accurate  $J$  results, however the bi-quadratic  $\varphi$  presents a more robust behavior. These behaviors for the two definitions of  $\varphi$  are the same as those reported in a recent paper by one of the authors of this work [15] when dealing with the application of the EDI to linear elastic crack problems without the presence of body loads.

## Acknowledgment

This work was financed by the Fondo Nacional de Ciencia y Tecnología de Venezuela (FONACIT) and by Grant No. PICT 12-12528 of the Agencia Nacional de Promoción Científica y Tecnológica de la República Argentina (ANPYCT).

## Appendix

In this appendix the fundamental solutions for the implementation of the thermoelastic formulation of the dual boundary element method are provided. In what follows the symbol  $r$  stands for the distance from the field point  $x$  to the source point  $x'$ :

$$r(x', x) = |x - x'| \quad (A1)$$

The notation  $r_{,k}$  indicates the derivative at the source point, i.e.,

$$\frac{\partial r}{\partial x_k} = -r_{,k} \quad (A2)$$

The fundamental solutions in the temperature Eq. (10) are

$$\theta^*(x', x) = \frac{-1}{4\pi r} \quad (A3)$$

$$q^*(x', x) = \lambda \frac{r_{,k} n_k}{4\pi r^2} \quad (A4)$$

The fundamental solutions for the flux Eq. (11) can be found after the differentiation of the solutions (A3) and (A4) to yield

$$\theta_i^{**}(x', x) = \frac{\lambda}{4\pi r^2} r_{,i} \quad (A5)$$

$$q_i^{**}(x', x) = \frac{\lambda}{4\pi r^3} (3r_{,i} r_{,k} n_k - n_i) \quad (A6)$$

The fundamental solutions in the displacement Eq. (14) are given by

$$T_{ij}(x', x) = \frac{-1}{8\pi(1-\nu)r^2} \left\{ \frac{\partial r}{\partial n} [(1-2\nu)\delta_{ij} + 3r_{,i}r_{,j}] - (1-2\nu)(n_j r_{,i} - n_i r_{,j}) \right\} \quad (A7)$$

$$U_{ij}(x', x) = \frac{-1}{16\pi(1-\nu)\mu r} \{ (3-4\nu)\delta_{ij} + r_{,i}r_{,j} \} \quad (A8)$$

$$\bar{P}_i(x', x) = \frac{\alpha(1+\nu)}{8\pi(1-\nu)r} \left( n_i - \frac{\partial r}{\partial n} r_{,i} \right) \quad (A9)$$

$$\bar{Q}_i(x', x) = \frac{\alpha(1+\nu)}{8\pi(1-\nu)r_{,i}} \quad (A10)$$

The fundamental solutions in the traction equation (15) are obtained by material constitutive relationships. This procedure results in

$$T_{kij}(x', x) = \frac{\mu}{4\pi(1-\nu)r^3} \left\{ 3 \frac{\partial r}{\partial n} [ (1-2\nu) \delta_{ij} r_{,k} + \nu (\delta_{ij} r_{,k} + \delta_{jk} r_{,i} - 5 r_{,i} r_{,j} r_{,k}) ] + 3\nu (n_i r_{,j} r_{,k} + n_j r_{,i} r_{,k}) + (1-2\nu) (3n_k r_{,i} r_{,j} + n_k \delta_{ij} + n_i \delta_{jk}) - (1-4\nu) n_k \delta_{ij} \right\} \quad (\text{A11})$$

$$U_{kij}(x', x) = \frac{1}{8\pi(1-\nu)r^2} [ (1-2\nu) (\delta_{ik} r_{,j} + \delta_{jk} r_{,i} - \delta_{ij} r_{,k}) + 3r_{,i} r_{,j} r_{,k} ] \quad (\text{A12})$$

$$\bar{P}_{ij}(x', x) = 4 \frac{\alpha\mu(1+\nu)}{8\pi(1-\nu)r^2} \left\{ n_k r_{,k} \left[ \frac{\delta_{ij}}{1-2\nu} - 3r_{,i} r_{,j} \right] + n_i r_{,j} + n_j r_{,i} \right\} \quad (\text{A13})$$

$$\bar{Q}_i(x', x) = 4 \frac{\alpha\mu(1+\nu)}{8\pi(1-\nu)r} \left( r_{,i} r_{,j} - \frac{\delta_{ij}}{1-2\nu} \right) \quad (\text{A14})$$

## References

- [1] *Stress Intensity Factor Handbook*, 1987, Y. Murakami, ed., Pergamon Press, Oxford, UK.
- [2] Tada, H., Paris, P. C., and Irwin, G. R., 2000, *The Stress Analysis of Cracks Handbook*, 3rd ed., ASME Press, New York.
- [3] Brebbia, C. A., Telles, J. C. F., and Wrobel, L. C., 1984, *Boundary Element Techniques*, Springer-Verlag, Berlin.
- [4] Aliabadi, M. H., 1997, "Boundary Element Formulations in Fracture Mechanics," *Appl. Mech. Rev.*, **50**, pp. 83–96.
- [5] Raveendra, S. T., and Banerjee, P. K., 1992, "Boundary Element Analysis of Cracks in Thermally Stressed Planar Structures," *Int. J. Solids Struct.*, **29**, pp. 2301–2317.
- [6] Mukherjee, Y. X., Shah, K., and Mukherjee, S., 1999, "Thermoelastic Fracture Mechanics with Regularized Hypersingular Boundary Integral Equations," *Eng. Anal. Boundary Elem.*, **23**, pp. 89–96.
- [7] Prasad, N. N. V., Aliabadi, M. H., and Rooke, D. P., 1994, "The Dual Boundary Element Method for Thermoelastic Crack Problems," *Int. J. Fract.*, **66**, pp. 255–272.
- [8] dell'Erba, D. N., and Aliabadi, M. H., 2001, "BEM Analysis of Fracture Problems in Three-Dimensional Thermoelasticity Using J-Integral," *Int. J. Solids Struct.*, **38**, pp. 4609–4630.
- [9] Aliabadi, M. H., and Rooke, D. P., 1992, *Numerical Fracture Mechanics*, Computational Mechanics Publications, Southampton, UK.
- [10] Kishimoto, K., Auki, S., and Sakata, M., 1980, "On the Path Independent Integral-J," *Eng. Fract. Mech.*, **13**, pp. 841–850.
- [11] Shih, C. F., Moran, B., and Nakamura, T., 1986, "Energy Release Rate Along a Three-Dimensional Crack Front in a Thermally Stressed Body," *Int. J. Fract.*, **30**, pp. 79–102.
- [12] Cislino, A. P., Aliabadi, M. H., and Otegui, J. L., 1998, "Energy Domain Integral Applied to Solve Center and Double-Edge Crack Problems in Three-Dimensions," *Theor. Appl. Fract. Mech.*, **29**, pp. 181–194.
- [13] Cislino, A. P., and Aliabadi, M. H., 1999, "BEM Implementation of the Energy Domain Integral for the Elastoplastic Analysis of 3D Fracture Problems," *Int. J. Electron.*, **96**, pp. 229–245.
- [14] Cislino, A. P., and Ortiz, J. E., 2005, "Three-Dimensional Boundary Element Assessment of Fibre/Matrix Interface Cracks Under Transverse Loading," *Comput. Struct.*, **83**, pp. 856–869.
- [15] Cislino, A. P., and Ortiz, J. E., 2005, "Boundary Element Analysis of Three-Dimensional Mixed-Mode Cracks via the Interaction Integral," *Comput. Methods Appl. Mech. Eng.*, **194**(11), pp. 935–956.
- [16] Natha, R., and Moran, B., 1993, "Domain Integrals for Axisymmetric Interface Crack Problems," *Int. J. Solids Struct.*, **30**(15), pp. 2027–2040.
- [17] Saliva, R., Vènere, M. J., Padra, C., Taroco, E., and Feijoo, R. A., 2000, "Shape Sensitivity Analysis and Energy Release Rate of Planar Cracks Embedded in Three-Dimensional Bodies," *Comput. Methods Appl. Mech. Eng.*, **188**, pp. 649–664.
- [18] Wilson, W. K., and Yu, I. W., 1979, "The Use of J-Integral in Thermal Stress Crack Problems," *Int. J. Fract.*, **15**, pp. 377–387.
- [19] Das, B. R., 1977, "Thermal Stress in a Long Cylinder Containing a Penny-Shaped Crack," *Int. J. Eng. Sci.*, **6**, pp. 497–516.